



Short communication

New easy way preparation of core/shell structured SnO₂@carbon spheres and application for lithium-ion batteries

Xuecheng Chen^{a,*}, Krzysztof Kierzek^b, Karolina Wilgosz^a, Jacek Machnikowski^b, Jiang Gong^c, Jingdong Feng^c, Tao Tang^c, Ryszard J. Kalenczuk^a, Hongmin Chen^d, Paul K. Chu^d, Ewa Mijowska^a

^a Institute of Chemical and Environment Engineering, West Pomeranian University of Technology, Szczecin, ul. Pulaskiego 10, 70-322 Szczecin, Poland

^b Department of Polymer and Carbonaceous Materials, Wrocław University of Technology, ul. Gdanska 7/9, 50344 Wrocław, Poland

^c Changchun Institute of Applied Chemistry, Chinese Academy of Science, Changchun, China

^d Department of Physics and Materials Science, City University of Hong Kong, Tat Chee Avenue, Kowloon, Hong Kong, China

HIGHLIGHTS

- Core/shell structures composed of tin oxide nanoparticles confined in mesoporous hollow carbon spheres are reported.
- The materials have a uniform size distribution, good structural stability, and large surface area.
- Core/shell structure exhibits superior cycling performance comparing with hollow carbon spheres.
- When the SnO₂/C ratio is 78.6/21.4 (w/w), the surface area of SnO₂@MHCS is 183 m² g⁻¹.
- The specific capacity value is 450 mAh g⁻¹ at 1/5 C after 50 cycles.

ARTICLE INFO

Article history:

Received 17 March 2012

Received in revised form

31 May 2012

Accepted 5 June 2012

Available online 12 June 2012

Keywords:

Core/shell

Hollow carbon spheres

Tin oxide

Lithium-ion battery

ABSTRACT

A novel way for the synthesis of core/shell structures composed of tin oxide nanoparticles confined in mesoporous hollow carbon spheres (SnO₂@MHCS) is newly reported. The materials which have a uniform size distribution, good structural stability and large surface area show superior cycling performance and are suitable for high-power anodes. Core/shell structured SnO₂@MHCS takes advantage of the virtues of SnO₂ and porous carbon in lithium-ion battery. This structure provides a rapid lithium transport pathway and boasts a highly reversible capacity. When the SnO₂/C ratio is 78.6/21.4 (w/w), the surface area of SnO₂@MHCS is 183 m² g⁻¹ and specific capacity value is 450 mAh g⁻¹ at 1/5 C after 50 cycles. The SnO₂@MHCS materials have large potential in next-generation lithium-ion batteries.

© 2012 Elsevier B.V. All rights reserved.

1. Introduction

Lithium-ion batteries have great potential in electric and hybrid vehicles due to their high electromotive force and high energy density. However, the rate performance needs improvement [1–3]. The lithium storage capacity in graphite is limited to the theoretical maximum capacity of 372 mAh g⁻¹. Therefore, considerable efforts have been devoted to identify alternative anode materials for lithium-ion batteries to improve to boost the capacity beyond this level. The report of SnO₂-based anode materials by Miyasaka and co-workers [4] has spurred interest in their applications to lithium-ion batteries due to the high theoretical specific lithium storage

capacity of 783 mAh g⁻¹, low cost, low toxicity, low potential of lithium-ion intercalation, as well as widespread availability [5–7]. Unfortunately, pure SnO₂ suffers from a large volume change during lithium alloying and de-alloying, thereby jeopardizing the mechanical integrity of SnO₂-based electrodes. As a result, the materials can be pulverized and the batteries composed of such materials encounter very rapid capacity fading during charging/discharging cycles [8–10]. Recent work has revealed a potential solution to this problem by utilizing hierarchically structured nanometer-scale SnO₂/carbon composites [11–13]. In these structures, the carbon matrix can accommodate the mechanical stress induced by the huge volume expansion and shrinkage of high-capacity SnO₂ during the lithium insertion/extraction processes thus minimizing deterioration and better preserving the integrity of the anodes [14].

* Corresponding author. Tel./fax: +48 91449486.

E-mail address: xchen@zut.edu.pl (X. Chen).

Graphitic carbon is the most commonly used anode materials in commercial lithium-ion batteries due to the high electrical conductivity, low cost, high yield, and long cycle lifetime. However, the low solid-state diffusion coefficient of lithium imposes a serious restriction [15] and improving the rate capability of graphitic materials is still a great challenge [16,17]. Recently, X. Chen et al. showed that mesoporous hollow carbon spheres (MHCS) could improve the rate capacity [18], thus providing a new opportunity to use graphitic materials in further functionalization. Nonetheless, direct use of the mesoporous hollow carbon structure is still a challenge, but combining SnO_2 and porous carbon to take advantage of the virtues of the two materials may be a viable alternative.

In the work reported in this paper, we found a new way to synthesize a core/shell structures consisting of SnO_2 nanoparticles confined in mesoporous hollow carbon spheres (SnO_2 @MHCS). It is totally different from most of the reported method, in these traditional methods, for the fabrication of core/shell nanoparticles, the nanoparticles to be encapsulated are first prepared followed by the fabrication of the outside layer [19,20]. Such procedures are relatively complex and the loading capacity of nanoparticles inside the macroporous core is relatively low. However, in our presented method, SnCl_2 used as a precursor directly diffuses into the MHCS via the mesoporous shell without previous chemical modification of carbon spheres. The excess precursor deposited onto the spheres can be easily washed away thus ensuring exclusive loading of the precursor inside the MHCS. After annealing, the metal salt is easily converted *in situ* into the corresponding metal oxide to produce the core/shell structured SnO_2 @MHCS. Therefore, the synthetic technique presented here has two main advantages. First of all, the macroporous core of the carbon capsules can be filled with a significant amount of SnO_2 nanoparticles [21,22] and secondly, this methodology can be expanded to encapsulate a variety of inorganic materials with the low volatility below the carbon oxidation temperatures. The properties of the core/shell nanostructure are evaluated from the viewpoint of lithium-ion batteries [23].

2. Experimental

The mesoporous hollow carbon spheres (250 mg, diameter = 300 nm, and wall thickness = 70 nm) were fabricated using the technique described in our previous paper [18]. The MHCS together with 1 g of $\text{SnCl}_2 \cdot 2\text{H}_2\text{O}$ and 5 ml of concentrated HCl were put inside a glass tube, sealed, and heated to 100 °C for 24 h. Afterward, the solution was evaporated during stirring and the dry powder collected was washed with ethanol several times to remove excess of SnCl_2 . Finally, the product was heated to 400 °C for 3 h to form the core/shell structured SnO_2 @MHCS.

X-ray diffraction (XRD) was conducted on a Philips diffractometer using $\text{Cu K}\alpha$ radiation. Transmission electron microscopy (TEM) and electron microscopy (TEM) were performed on the FEI Tecnai F30 transmission electron microscope with a field emission gun operating at 200 kV to examine the dimensions and structural details of the core-shell nanoparticles. The N_2 adsorption/desorption isotherms were acquired at liquid nitrogen temperature (77 K) using a Micromeritics ASAP 2010M instrument and the specific surface area was calculated by the Brunauer–Emmett–Teller (BET) method. The pore size distribution was determined using the Barret–Joner–Halenda (BJH) method. Raman scattering was conducted on a Renishaw micro Raman spectrometer ($\lambda = 514 \text{ nm}$). The thermogravimetric analysis (TGA) was carried out on 10 mg samples on the DTA-Q600 SDT TA at a heating rate of $10^\circ\text{C min}^{-1}$ from room temperature to 900 °C under flowing air.

The electrochemical experiments were carried out using 2032 coin-type cells. The working electrodes were prepared by mixing

the hollow carbon spheres, carbon black (C-ENERGY™ SUPER C65, Timcal), and polyvinylidene difluoride (PVDF, Solef 5130, Solvay) at a weight ratio of 80:10:10 and pasting onto Cu foils (Schlenk Metallfolien GmbH & Co.). A lithium foil (Aldrich) was used as the counter electrode. The electrolyte consisted of a solution of 1 M LiPF_6 in ethylene carbonate (EC)/dimethyl carbonate (DMC) (1:1 by volume) obtained from Merck Chemicals (SelectiLyte™ LP30). The cells were assembled in an argon-filled glove box with less than 1 ppm moisture and oxygen. The electrochemical performance was evaluated in the voltage range of 0.005–2.0 V by using a galvanostatic charge/discharge and cycling voltammetry techniques.

3. Results and discussion

Fig. 1 illustrates the procedures to prepare the core/shell structured SnO_2 @MHCS. The mesoporous hollow carbon spheres are first soaked in a mixture of SnCl_2 and HCl at 100 °C for 24 h in a sealed glass tube and SnCl_2 can easily diffuse into the hollow cavity through the mesoporous channels. After heating in air at 400 °C for 3 h, SnCl_2 was changed to SnO_2 *in situ*. Finally, mesoporous SnO_2 was formed inside mesoporous hollow carbon spheres.

The morphology of the original mesoporous hollow carbon spheres is characterized by transmission electron microscopy. As shown in Fig. 2(a) and (b), the hollow carbon spheres are very uniform with a diameter of about 300 nm and the shell has a thickness of about 70 nm. From Fig. 2(b), the through channels direct to the hollow core are clearly observed. These MHCS have a large surface area of $771 \text{ m}^2 \text{ g}^{-1}$ and pore size in the range of 2–7 nm, both of which are large enough to provide easy access to the internal void space. The morphology of core/shell SnO_2 @MHCS in Fig. 2(c) and (d) shows that the dark inner part of the sphere corresponding to SnO_2 nanoparticles is confined in the cavity of the hollow carbon spheres. From these TEM images, we can say that SnCl_2 was successfully introduced into the hollow carbon spheres and converted to SnO_2 by heating process in air. Another experiment that SnCl_2 heated in air at 400 °C for 3 h was done, finally only white powder appeared, which was attached to the inner space of the tube furnace. Because SnCl_2 is easy to evaporate at high temperature and SnCl_2 gas was changed to SnCl_2 powder in low temperature area. Comparing to aforementioned two experiment results, mesoporous hollow carbon sphere can provide the confined effect for the SnCl_2 , it made SnCl_2 change to SnO_2 nanoparticles. Fig. 2(e) and (f) shows the SnO_2 nanoparticles in the mesoporous carbon shell (as indicated by black arrows) and in the core (as indicated by white arrows). The size of SnO_2 nanoparticles in the carbon shell is about 5 nm and the size of SnO_2 nanoparticles in the core is about 9 nm.

According to a reported technique, the mesoporous hollow silica spheres and melted SnCl_2 were mixed at 100 °C and heated at 600 °C to form SnO_2 hollow spheres [24]. Based on this idea, the same experiments were also done for mesoporous carbon sphere and SnCl_2 . However, we could not get satisfactory results. As shown in Fig. 3, most of SnO_2 nanoparticles are dispersed outside the hollow carbon spheres and only little SnCl_2 get into the mesoporous

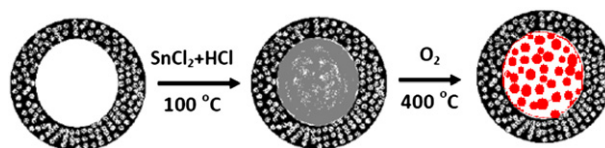


Fig. 1. Schematic illustration of the synthetic procedure to produce the core-shell SnO_2 @MHCS.

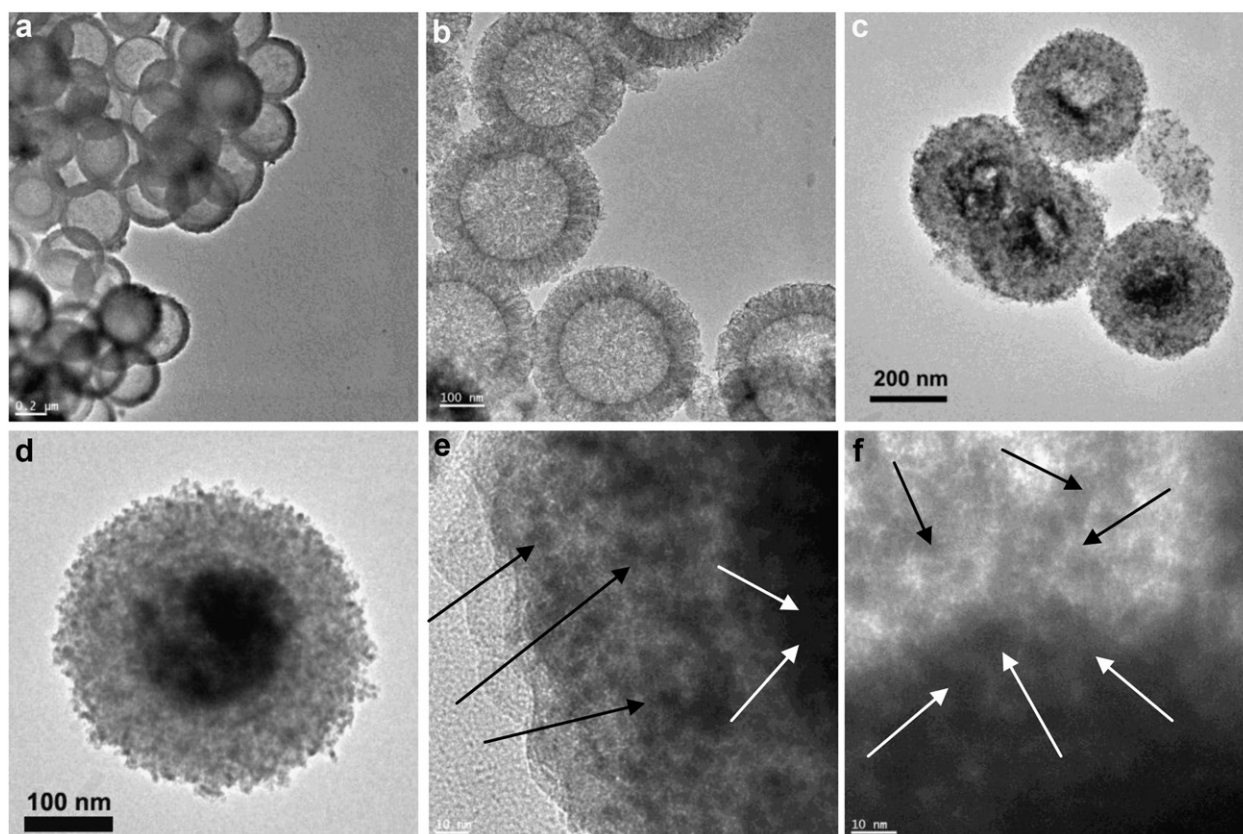


Fig. 2. (a, b) TEM image of mesoporous hollow carbon spheres. (c, d) TEM images of SnO_2 in mesoporous carbon hollow spheres. (e) SnO_2 nanoparticles in the carbon shell (black arrows) and (f) SnO_2 nanoparticles (white arrows) in the core.

shell of the hollow carbon spheres. Therefore, a different technique described above was adopted in our experiments.

The X-ray diffraction (XRD) pattern of MHCS in Fig. 4(a) shows strong diffraction peaks at 24.9° (2θ) and 42° (2θ), which are ascribed to graphitic carbon. Formation of encapsulated SnO_2 inside the hollow carbon spheres is indicated by the red line showing peaks with 2θ values of 26.97° , 34.34° , 38.26° , 52.01° , 54.90° , 58° , 62° , and 64.9° , corresponding to the SnO_2 tetragonal rutile crystal planes of (110), (101), (200), (211), (220), (002), (310) and (301), respectively (JCPDS-PDF#021-1250) (ICSD data)

(Fig. 4(b)) [25]. (For interpretation of the references to color in this figure legend, the reader is referred to the web version of this article.) The XRD patterns in Fig. 4(b) indicate that the encapsulated SnO_2 phases are well-crystallized and in general, the encapsulated inorganic phase consists of an agglomeration of nanoparticles. From Scherrer equation, the mean size of SnO_2 nanoparticles inside of hollow carbon spheres is 8 nm.

TGA measurements (Fig. 5(a)) provide information about the carbon content as well as quality of the hollow carbon spheres, because the oxidation temperature affects the wall defects. Ideal

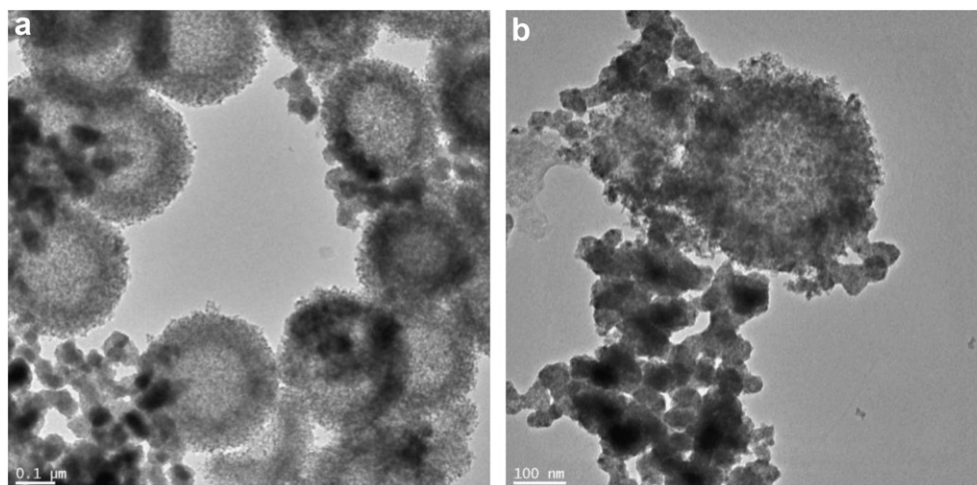


Fig. 3. Melting method synthesis of SnO_2 @MHCS.

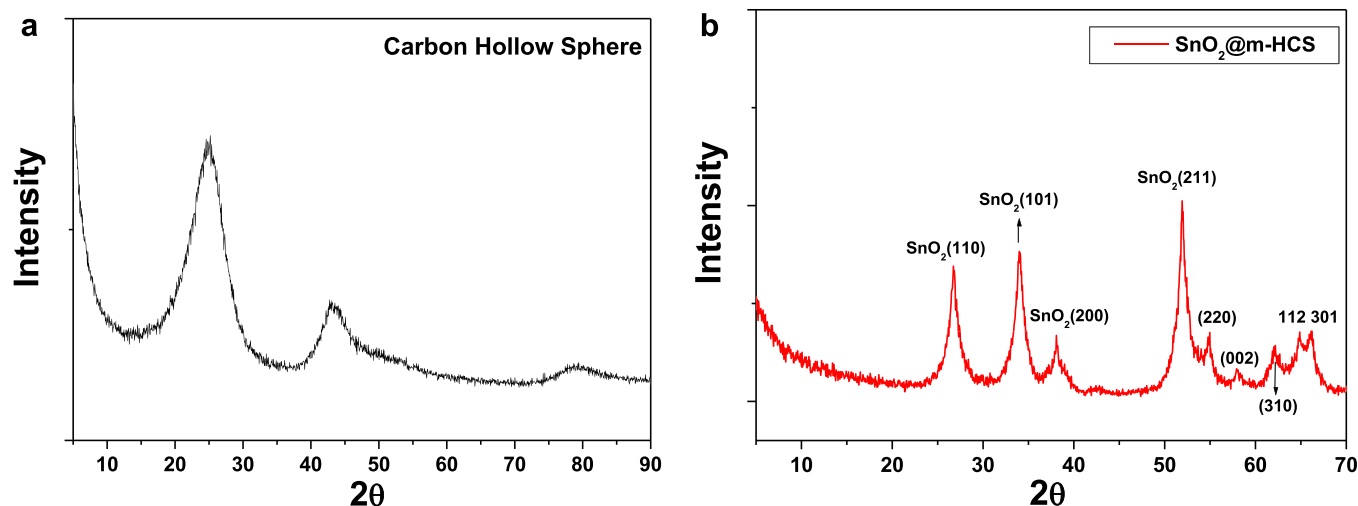


Fig. 4. XRD patterns of (a) MHCS and (b) core/shell SnO_2 @MHCS.

graphite starts to oxidize at above 600 °C, whereas the hollow carbon spheres are oxidized at above 500 °C. The hollow carbon spheres begin to decompose at 586 °C in air. As the temperature is further increased, the weight loss increases rapidly until all the carbon spheres are exhausted at about 707 °C. The ash content of the hollow carbon spheres after combustion at 900 °C is 0% w/w implying that the produced hollow carbon spheres have high purity. The core/shell SnO_2 @MHCS exhibits a similar TGA behavior under these experimental conditions. However, larger amounts of residue are obtained from the core/shell SnO_2 @MHCS than MHCS at temperature between 580 °C and 900 °C. The change in the TGA residue at 900 °C is also apparent in Fig. 5(a) for the pure hollow

carbon spheres (0% w/w) and core/shell SnO_2 @MHCS (76.8% w/w). Hence the content of SnO_2 in the core/shell SnO_2 @MHCS is about 76.8% w/w. From Fig. 5(a), TGA profile of SnO_2 @MHCS, from room temperature to 500 °C, there is almost no weight change, so we are sure that $\text{SnCl}_2 \rightarrow \text{SnO}_2$ transformation is finished. Nitrogen isothermal adsorption–desorption is performed to determine the pore structure and Brunauer–Emmett–Teller (BET) surface areas of both the MHCS and SnO_2 @MHCS. Fig. 5(b) and (c) displays the typical IV isotherms of a mesoporous structure of MHCS and SnO_2 @MHCS. The BET surface area is 771 $\text{m}^2 \text{g}^{-1}$ for MHCS and 183.8 $\text{m}^2 \text{g}^{-1}$ for SnO_2 @MHCS. The significant decrease in the BET surface area also confirms loading of SnO_2 inside MHCS and the

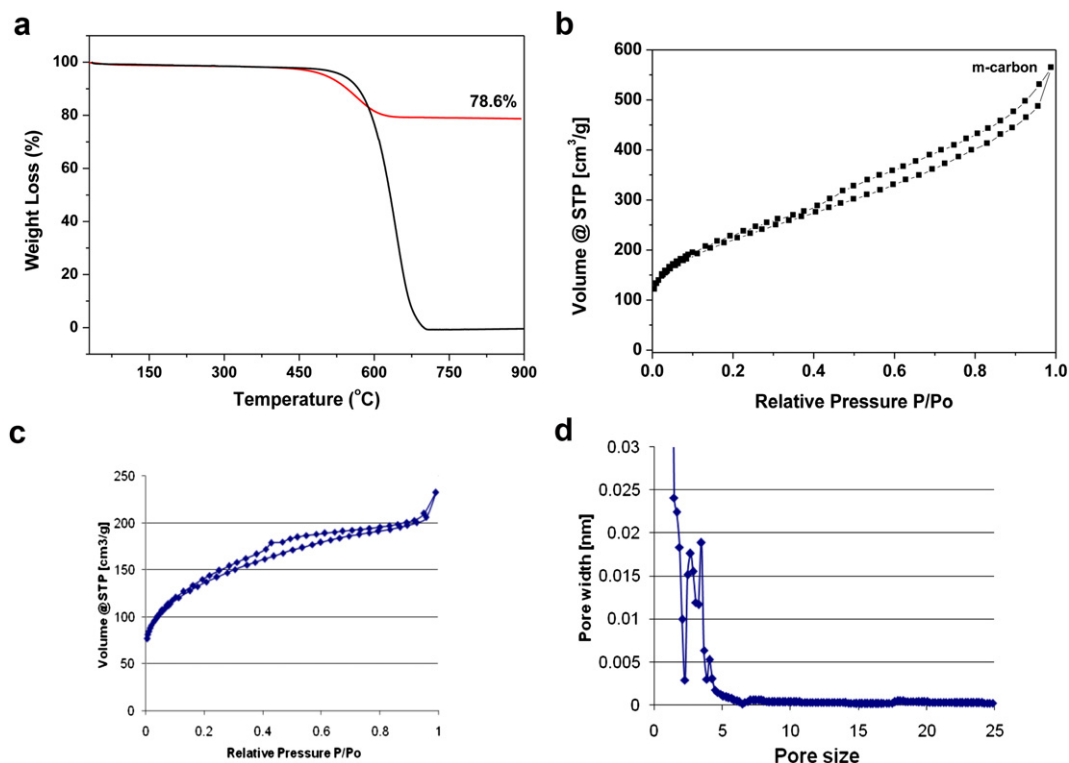


Fig. 5. (a) TGA curves of MHCS and SnO_2 @MHCS. (b) N_2 adsorption/desorption isotherms of MHCS and SnO_2 @MHCS (c). (d) Pore size distribution of SnO_2 @MHCS.

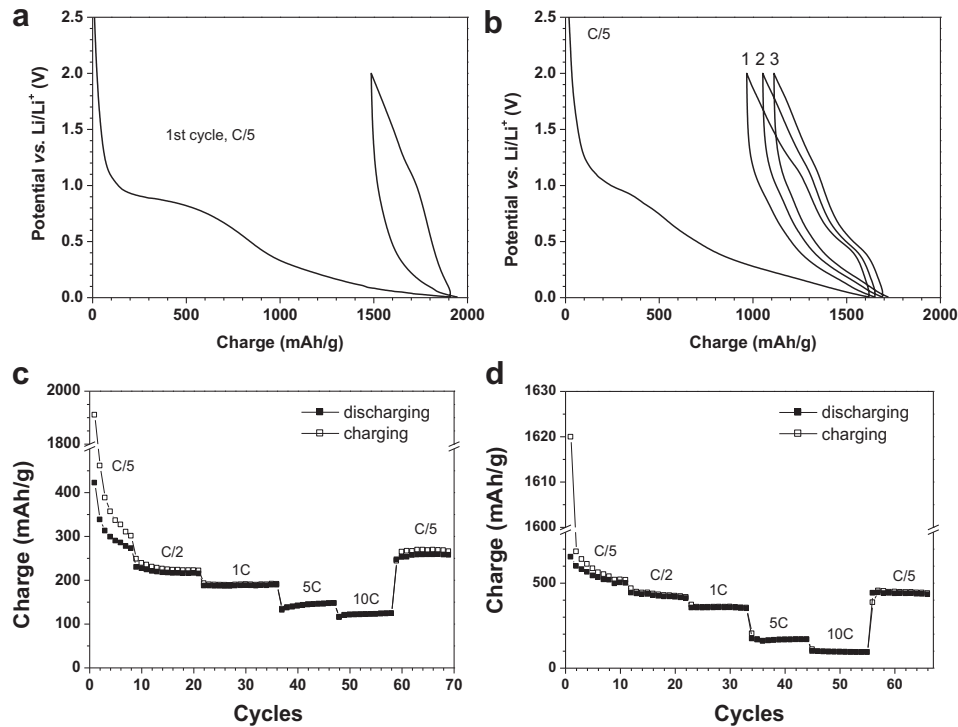


Fig. 6. Lithium storage properties of the as-prepared carbon hollow nanospheres and $\text{SnO}_2\text{@MHCS}$: (a, b) charge–discharge profiles and (c, d) cycling performance. All of the measurements are conducted at a current rate of 160 mA g^{-1} and voltage window of $0.01\text{--}2.0 \text{ V}$ (76.8 wt\% SnO_2).

pore size distributions are shown in Fig. 5(d), the pore sizes are centered at 2.6 and 3.4 nm .

To reveal the advantage of the core/shell $\text{SnO}_2\text{@MHCS}$, we compare the lithium storage properties of the core/shell

$\text{SnO}_2\text{@MHCS}$ to those of the pure MHCS. Fig. 6 shows that the $\text{SnO}_2\text{@MHCS}$ composite materials have the improved cyclability as an anodic material in Li-ion battery. As shown in Fig. 6(a) and (b), for $\text{SnO}_2\text{@MHCS}$, the first charge capacity is 1619 mAh g^{-1} , which is

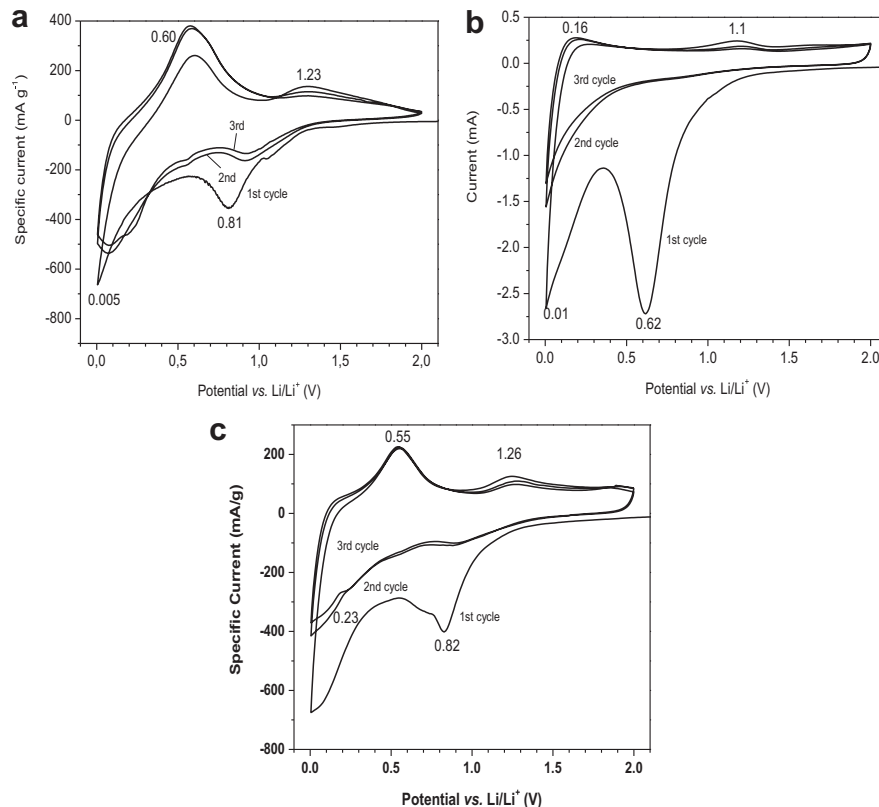


Fig. 7. Cycling voltammetry profile of (a) MHCS and (b) $\text{SnO}_2\text{@MHCS}$ electrode (potential range: $0.005\text{--}2 \text{ V}$ vs. Li/Li^+ , scan rate: 0.1 mV s^{-1}).

lower than that of pure hollow carbon spheres of 1908 mAh g⁻¹ at a rate of C/5 (Fig. 6(a) and (b)). This is higher than that reported for graphite (372 mAh g⁻¹). A large irreversible capacity of about 967 mAh g⁻¹ is also observed from the SnO₂@MHCS and it is lower than that of the hollow carbon spheres (1489 mAh g⁻¹) during the first discharging and charging processes (Fig. 6(b)). The cycling performance of the as-prepared MHCS and SnO₂@MHCS up to 50 cycles is shown in Fig. 6(c) and (d). The as-prepared SnO₂@MHCS materials show very good performance. In fact, the low initial coulombic efficiency is a common phenomenon for porous carbonaceous electrodes in lithium-ion batteries. This can result in the decomposition of electrolyte and formation of the solid/electrolyte interphase (SEI) films at the electrode/electrolyte interface. The performance of the hollow carbon spheres is presented in Fig. 6(c). The reversible capacity is stable at 268 mAh g⁻¹ and 450 mAh g⁻¹ for MHCS and SnO₂@MHCS after 50 cycles at a rate of C/5. This proved that the incorporation of SnO₂ into hollow carbon spheres increased the improved cyclability compare to pure hollow carbon spheres. With regard to SnO₂@MHCS, after increasing the discharge/charge rates to 1C and 5C, the reversible capacity is maintained at 189 and 145 mAh g⁻¹, respectively. In addition, the high-rate cycling performance of the core/shell structured SnO₂@MHCS is noteworthy. For example, after 60 cycles, the retention of the reversible capacity at 10C is nearly 100%, this is the character inherited from hollow carbon spheres. A possible reason for the MHCS and SnO₂@MHCS having a higher lithium storage capacity is the internal void space which stores more lithium.

The lithium insertion/extraction processes in the SnO₂ nanoparticles, MHCS and SnO₂@MHCS nanospheres are further characterized by cyclic voltammetry (CV) in Fig. 7, it shows the CV profiles of the first three cycles at a scanning rate of 0.05 mV s⁻¹ and potential window of 2 V–5 mV. The CV experiment was also applied to anode prepared from SnO₂ nanoparticles as reference material. Fig. 7(a) shows the CV profiles of the first three cycles of SnO₂. A cathodic peak at 0.81 V can be attributed to the solid electrolyte interphase (SEI) formation on the external surface of the material. The reaction of electrochemical reducing of SnO₂ nanoparticles ($4\text{Li}^+ + \text{SnO}_2 + 4\text{e}^- \rightarrow \text{Sn} + \text{Li}_2\text{O}$) [26,27] and lithium insertion to the *in-situ* obtained tin ($x\text{Li}^+ + \text{Sn} + x\text{e}^- \rightarrow \text{Li}_x\text{Sn}$), start below 0.7 V and escalate up to discharge cut-off potential (0.005 V). The 0.60 V oxidation peak can be assigned to the de-alloying of whereas the weak oxidation peak at 1.23 V is due to the partly reversible reaction $4\text{Li}^+ + \text{SnO}_2 + 4\text{e}^- \rightarrow \text{Sn} + \text{Li}_2\text{O}$. The de-alloying process is intensified in the second cycle, as an effect of higher saturation of active material with lithium during cathodic sweep. As shown in Fig. 7(b), for MHCS, in the first cycle, there is also a strong cathodic peak at 0.62 V arising from the formation of the SEI. The peak at 0.01 V is ascribed to lithium insertion into the graphene nanosheets which come from the mesoporous wall of the carbon hollow spheres. There is one oxidation peak at 0.16 V corresponding to lithium extraction from graphene nanosheet ($x\text{Li}^+ + \text{C}(\text{graphene}) + x\text{e}^- \rightarrow \text{Li}_x\text{C}$). This peak can be only found in graphene related materials. The CV curves of SnO₂@MHCS seem to be an superimposition of current response of separated SnO₂ and MHCS (Fig. 7(c)). In the first cycle, there is a strong bimodal signal in the range of 0.5–1.2 V in the cathodic sweep, what is effect of overlapped peaks, attributed to the formation of the SEI layer on the SnO₂ (at 0.83 V) and MHCS phase (at 0.65 V). The other reduction process placed below 0.5 V can be obviously ascribed to the lithium reaction with SnO₂ and insertion in graphene nanosheets [28,29]. Three oxidation peaks appear at around 0.16, 0.55 and 1.23 V, correspond to lithium extraction from the graphene nanosheet, de-alloying of Li_xSn and reversible tin oxidation, respectively. The CV measurements clearly reveal the reversible electrochemical reactions between lithium ions and the SnO₂@MHCS carbon spheres in

the lithium-ion cells. For the SnO₂ nanoparticles encapsulated by MHCS, the nanosized SnO₂ contacted with graphite sheet ensures a good conductivity, the loosely dispersed SnO₂ nanoparticles inside MHCS and the hollow structure can provide the some space to buffer parts of the volume change during the Li-ion insertion and extraction reactions in SnO₂ nanoparticles. All of these factors above-mentioned can enhance the cycle ability of SnO₂@MHCS composite material.

Compared to the MHCS, introduction of SnO₂ nanoparticles into the inner space of MHCS enhances the lithium storage properties such as first charge–discharge capacity and cycling performance. The SnO₂@MHCS not only retains the advantages of mesoporous hollow carbon spheres (for example, the hollow structure provides void volume to compensate for the parts of the volume expansion during Li⁺ insertion, high lithium storage density from the mesoporous shell, and high-rate cycling performance), but also the high lithium storage capacity of SnO₂. Combining the virtues of SnO₂ and MHCS, the lithium-ion battery performance of the SnO₂@MHCS is better than that of the MHCS.

4. Conclusions

SnO₂ nanoparticles are incorporated into mesoporous hollow carbon spheres by a simple process. The elastic hollow structure with SnO₂ nanoparticles inside exhibits superior cycling performance comparing with hollow carbon spheres. This structure is suitable for high-power anode materials and the hollow structure creates a rapid lithium transport pathways to facilitate the C-rate capability and has a highly reversible capacity. When the SnO₂/C ratio is 78.6/21.4 (w/w), the surface area of SnO₂@MHCS is 183 m² g⁻¹ and specific capacity value is 450 mAh g⁻¹ at 1/5 C after 50 cycles. As a result, the SnO₂@MHCS materials are promising candidates in next-generation lithium-ion batteries.

References

- [1] K.S. Kang, Y.S. Meng, J. Breger, C.P. Grey, G. Ceder, *Science* 311 (2006) 977–980.
- [2] Y. Wang, Y. Cao, *Adv. Mater.* 20 (2008) 2251–2269.
- [3] C.K. Chan, X.F. Zhang, Y. Cui, *Nano. Lett.* 8 (1) (2008) 307–309.
- [4] Y. Idota, T. Kubota, A. Matsufuji, Y. Maekawa, T. Miyasaka, *Science* 276 (1997) 1395–1397.
- [5] Y. Wang, J. Lee, *J. Phys. Chem. B* 108 (2004) 17832–17837.
- [6] P. Bueno, E. Leite, T. Giraldi, L. Bullhøes, E. Longo, *J. Phys. Chem. B* 107 (2003) 8878–8883.
- [7] X.W. Lou, Y. Wang, C. Yuan, J. Lee, L. Archer, *Adv. Mater.* 18 (2006) 2325–2329.
- [8] M.G. Kim, J. Cho, *Adv. Funct. Mater.* 19 (2009) 1497–1514.
- [9] F. Cheng, Z. Tao, J. Liang, J. Chen, *Chem. Mater.* 20 (2008) 667–681.
- [10] X.W. Lou, C.M. Li, L. Archer, *Adv. Mater.* 21 (2009) 2536–2539.
- [11] R. Demir-Cakan, Y.S. Hu, M. Antonietti, J. Maier, M.M. Titirici, *Chem. Mater.* 20 (2008) 1227–1229.
- [12] M. Noh, Y. Kwon, H. Lee, J. Cho, Y. Kim, M.G. Kim, *Chem. Mater.* 17 (2005) 1926–1929.
- [13] H.X. Zhang, C. Feng, Y.C. Zhai, K.L. Jiang, Q.Q. Li, S.S. Fan, *Adv. Mater.* 21 (2009) 2299–2304.
- [14] L.W. Ji, Z. Lin, B.K. Guo, A. Medford, J. Zhang, *Chem. Eur. J.* 16 (2010) 11543–11548.
- [15] W.M. Zhang, J.S. Hu, Y.G. Guo, S.F. Zheng, L.S. Zhong, W.G. Song, *Adv. Mater.* 20 (2008) 1160–1165.
- [16] K.T. Lee, J.C. Lytle, N.S. Ergang, S.M. Oh, A. Stein, *Adv. Funct. Mater.* 15 (2005) 547–556.
- [17] S.B. Yang, X.L. Feng, L.J. Zhi, Q. Cao, J. Maier, K. Müllen, *Adv. Mater.* 22 (2010) 838–842.
- [18] X.C. Chen, K. Kierzek, Z.W. Jiang, H.M. Chen, T. Tang, M. Wojtoniszak, *J. Phys. Chem. C* 115 (2011) 17717–17724.
- [19] L.M. Liz-Marzan, M. Giersig, P. Mulvaney, *Langmuir* 12 (1996) 4329–4335.
- [20] Y. Lu, Y.D. Yin, Z.Y. Li, Y.A. Xia, *Nano Lett.* 2 (2002) 785–788.
- [21] S. Ikeda, S. Ishino, T. Harada, N. Okamoto, T. Sakata, H. Mori, *Angew. Chem. Int. Ed.* 45 (2006) 7063–7066.
- [22] Y.H. Ng, S. Ikeda, T. Harada, S. Higashida, T. Sakata, H. Mori, *Adv. Mater.* 19 (2007) 597–601.
- [23] A.B. Fuertes, M. Sevilla, T. Valdes-Solis, P. Tartaj, *Chem. Mater.* 19 (2007) 5418–5423.

- [24] S.J. Ding, J.S. Chen, G.G. Qi, X.N. Duan, Z.Y. Wang, E.P. Giannelis, J. Am. Chem. Soc. 133 (2011) 21–23.
- [25] Joint Committee on Powder Diffraction Standards, Powder Diffraction File PDF# 021-1250.
- [26] P. Poizot, S. Laruelle, S. Grugeon, L. Dupont, J.M. Tarascon, Nature 407 (2000) 296.
- [27] J. Yao, X.P. Shen, B. Wang, H.K. Liu, G.X. Wang, Electrochem. Commun. 11 (2009) 1849–1852.
- [28] A. Fernández, F. Martín, J. Morales, J.R. Ramos-Barrado, L. Sánchez, Electrochim. Acta 51 (2006) 3391–3398.
- [29] Z.H. Wen, Q. Wang, Q. Zhang, J.H. Li, Adv. Funct. Mater. 17 (2007) 2772–2778.